ARMA 21–1958

Hydrogeological and Geomechanical Evaluation of a Shallow Hydraulic Fracture at the Devine Fracture Pilot Site, Medina County, Texas

Haddad*, M., Ahmadian*, M., Ge, J., Hosseini, S., Nicot, J.-P., Ambrose, W.

Bureau of Economic Geology, Jackson School of Geosciences, The University of Texas at Austin, Austin, Texas, USA

* *Corresponding Authors*

ABSTRACT: UT-Austin's Devine Fracture Pilot Site (DFPS), 50 miles southwest of San Antonio, Texas, has been targeted for a comprehensive, multidisciplinary development of fracture diagnostics techniques cross-validated by ground-truth data acquisition near a recently created, 175-ft-deep, horizontal hydraulic fracture. To evaluate the fracture-diagnostic techniques at this site, we attempted to develop hydrogeological and geomechanical models on the basis of bottomhole-pressure measurements during injection tests with a predefined volumetric flow-rate profile, resembling a diagnostic fracture injection test (DFIT). History-matching efforts using a simplified layer-cake hydrogeological model resulted in the field-scale formation permeability of 9.87×10^{-15}-m^2 (10-mD) and Darcy-scale fracture permeability. Analysis of bottomhole pressure and injection-rate history showed that (1) the preexisting horizontal fracture was closed adjacent to the injection well and (2) the initial pump-pressure increase at a negligible volumetric injection rate led to near-well fracture reopening, conductivity increase, and abrupt injection-rate increase. To overcome hydrogeological-model limitations of predicting fracture reopening throughout injection, we extended the modeling to a finite-element, poroelastic analysis of horizontal-fracture growth using a cohesive-zone model. Using this fracture-reopening model, we were able to match the transient-pressure response during the entire experiment by adjusting the hydromechanical properties. The current study lays the foundation for future work that our team will be performing at this well-characterized fracture site.

1. INTRODUCTION

Production from unconventional reservoirs has become economically feasible in the past 2 decades through multistage, hydraulic fracture stimulations along horizontal wells. This production depends on hydraulic-fracture dimensions that cannot be addressed only through near-well diagnostic techniques. Therefore, far-field surveys such as microseismic monitoring, tilt-meter mapping, shear-wave imaging, and electromagnetic tomography have been developed to characterize hydraulic fractures away from horizontal wells (Cipolla and Wright, 2000, Denison et al., 2015; Hu et al., 2016, 2018; LaBrecque et al., 2016; Haddad et al., 2017; Ahmadian et al., 2018, 2019; Fang et al., 2019; Stolyarov et al., 2019).

To evaluate the performance of an electromagnetically active proppant (EAP) in assisting with the geophysical tomography of hydraulic fracture networks, we previously developed and mapped a shallow horizontal fracture at the Devine Fracture Pilot Site (DFPS) in Medina County, Texas (Ahmadian et al., 2018). Next, our electromagnetic (EM) inversion-model predictions were validated by drilling and coring of multiple wells within the interpreted fracture zone and by induction logging, which revealed that the boundaries of EAPs matched very well with our model predictions (Ahmadian et al., 2019).

In this study, we have utilized our well-characterized, proppant-filled fracture anomaly at the DFPS to develop initial hydrogeological and geomechanical models with the following goals: (1) to evaluate the capability of these models in prediction of bottomhole pressure (BHP), fracture reopening and propped width, and salinity transport during fluid injection; (2) to calibrate the hydromechanical properties of the formation through history matching; and (3) to use these computational tools for design of the future injection scenarios at the DFPS.

Each of the two models have exclusive modeling capabilities that are essential for injection experiments. Because of poroelastic stress changes, hydraulic-fracture conductivity can change over the fracture footprint and through time. These changes are hard to predict using hydrogeological models, whereas our geomechanical model can overcome this limitation by solving for spatiotemporal fracture opening and poroelastic stresses and strains. On the other hand, a hydrogeological model can rigorously solve for salinity and species transport, which are not possible by a geomechanical model.

In this paper, we first address the uncertainty in our hydrogeological parameters through a set of field injections and by performing a comprehensive history-matching study. We obtained an optimal combination of formation permeability and spatiotemporal fracture permeability to match the modeled BHP with the field data. Then, we expanded the input parameter domain to the geomechanical properties and developed a poroelastic model to address the uncertainty in these parameters through history matching the BHP during fracture reopening. The geomechanical properties that were tuned are the initially open hydraulic-fracture area, fracture-initiation stress, and overburden-stress gradient.

2. FIELD EXPERIMENTS

In September 2020, we conducted three freshwater injection attempts at the DFPS. During these attempts, we pumped water into the perforations at a 53.34-m (175-ft) depth, where we had previously placed a horizontal, hydraulic fracture in 2017. Cores retrieved from the drilled wells at the DFPS were used for geological description of the near-surface formation at this injection site: tidal-flat, tidally influenced embayment, as well as a crevasse splay and splay channel in a deltaic setting (**Fig. 1**). Stratigraphy at the fracture depth of 53.34 m (175 ft) comprises a mixture of fine-grained sandstone and mudstone.

To characterize the formation and preexisting horizontal hydraulic fracture, we monitored and recorded the wellhead pressure, BHP, and volumetric injection rate during the operations. We used analog wellhead pressure gauges and deployed digital *In-Situ*™ transducers in the injection well, Devine Monitoring Well (DMW) 1, and DMW 2 (**Fig. 2**). These *In-Situ*™ transducers were positioned at either the perforated zone in the injection well or adjacent to the previously screened and gravel-packed regions in DMW 1 and 2 at the fracture depth. BHP changes during all these cycles agree with event logs and analog wellhead-pressure gauges.

Digitally recorded pressure profiles at the injection well and DMW 1 and 2 are shown in **Fig. 3**. We can specify seven exclusive time intervals in our field experiments: (1) partly successful injection attempt on September 22 (i.e., Cycle 0), (2) first successful injection attempt on September 23 (i.e., Cycle 1), (3) first shut-in for a short period beginning September 23 and ending September 24, (4) water extraction using an electric submersible pump (ESP) on September 24, (5) post-extraction period, (6) second successful injection attempt on September 25 (i.e., Cycle 2), and (7) extended shut-in from September 25 through 28. Retrieval and deployment of pressure transducers, which were conducted several times during the experiment, are reflected by stepwise pressure changes (e.g., on September 24 at 8 a.m. and September 26 at 9 a.m.) to the barometric pressure of 97.95 kPa (14.2 psi).

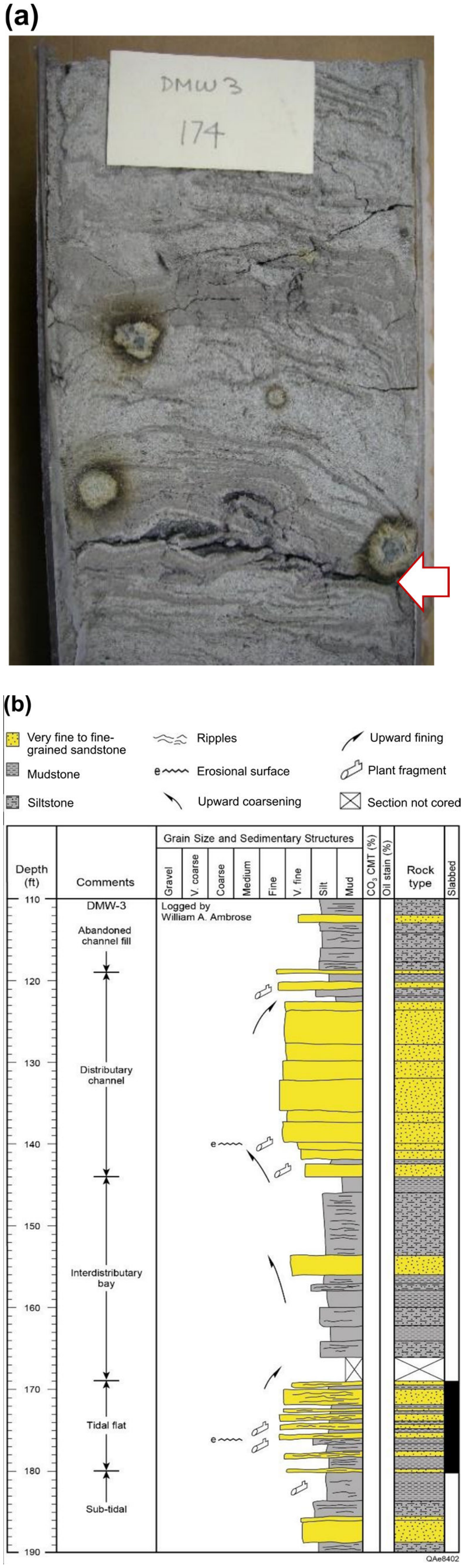

Fig. 1. (a) Representative core from Devine Monitoring Well (DMW) 3 at 53.04 m (174 ft) depth; white arrow marks the position of EAP containing fracture at 53.3 m (175 ft) depth; core tag 1 × 2 inches across. (b) Description and interpretation of core retrieved from depth interval of 33.53–57.91 m (110–190 ft) in DMW 3.

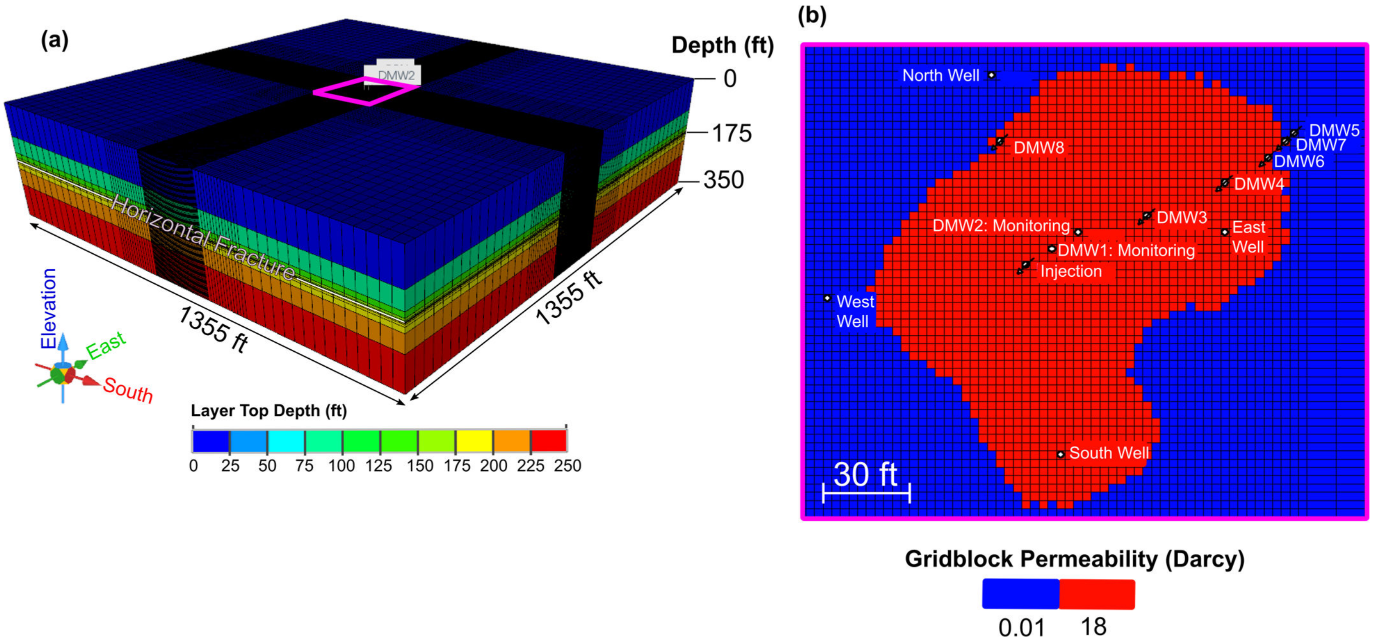

Fig. 2. Schematics of layer-cake hydrogeological model and gridding system: (a) 3D view; (b) an areal view of model at 53.34-m (175-ft) depth within purple rectangle in a. Horizontal, propped, hydraulic fracture shown by red domain at 1.78×10^{-11} m^2 (18 Darcy) permeability. DMW in b stands for Devine Monitoring Well. These wells lie along a radius in the northeast and at various distances from the injection well. DMW 1 is closest, at a distance of 3.05 m (10 ft) from the injection well.

Cycle 0 was only *partly* successful because of an injection-packer failure. During this cycle, small flow rates below a minimum measurable value of 6.309×10^{-5} m^3/s (1 GPM) were observed by a totalizer that was installed in the surface line. Although we did not observe an appreciable flow in the totalizer during Cycle 0, the increase in water levels in DMW 1 and 2 suggests that some fluid flow took place during this injection through a fracture-flow path between the injection well and DMW 1. To overcome the inflatable straddle packer failure, we installed a bridge plug at a 58.52-m (192-ft) depth and proceeded with Cycles 1 and 2.

Injection Cycles 1 and 2 occurred on September 23 and September 25 (**Fig. 3**). Cycle 1 started at 16:19 with flow rate and pressure going through a stepwise increase to a maximum flow rate of 2.208×10^{-4} m^3/s (3.5 GPM) and a wellhead pressure of 1.138 MPa (165 psi) in 1 hour and 15 minutes. After almost 2.5 hours of injection, the pump was shut in at 18:53, and the wellhead shutoff valve at the wellhead assembly was closed. Between the time intervals of 16:37 and 20:47, the hydraulic fracture was expected to remain dilated at the injection well. During Cycle 2, we repeated the water-injection process of Cycle 1, except for a maximum flow rate that was larger than that of Cycle 1. Cycle 2 started at 10:23 with the flow rate of 2.650×10^{-4} m^3/s (4.2 GPM) for almost 2 hours. At 12:11, we started to perform a stepwise increase in the flow rate up to 4.416×10^{-4} m^3/s (7 GPM) in 42 minutes. At 12:53, we started to gradually reduce the flow rate to zero in 42 minutes. Injection was followed by shutoff-valve closure and monitoring of BHP until September 28. BHP exceeded fracture-closure pressure (FCP; section 3.5) at 10:30 and 10:48 at the injection well and DMW 1, respectively, suggesting a gradual, radial reopening of the horizontal hydraulic fracture throughout injection. As a fracture characteristic, a maximum injection pressure of 1.97 MPa (285.3 psi) during this injection experiment was close to that of 1.93 MPa (280.3 psi) during the first successful injection cycle of September 23.

Time intervals 2 and 6, associated with injection Cycles 1 and 2, were separated by a short shut-in period, an extraction period, and a post-extraction period corresponding to time intervals 3, 4, and 5 (**Fig. 3**). These intermediate periods were intended to return the reservoir pressure to the initial pressure after the first injection period and repeat the injection experiment with identical initial conditions. A comparison of the original BHP of 241.469 kPa (35 psi; section 3.5) with the BHP after 3 days of shut-in without extraction on September 28 and BHP prior to the second successful injection on September 25 illustrated the substantial effect of extraction on reservoir-pressure drop. After 3 days of shut-in on September 28, BHP plateaued at 292.46 kPa (42.4 psi; Fig. 3), which is only 48.28 kPa (7 psi) higher than the original BHP. In addition, water extraction on September 24 led to a BHP of 251.76 kPa (36.5 psi; Fig. 3), which is only 6.90 kPa (1 psi) above the original BHP.

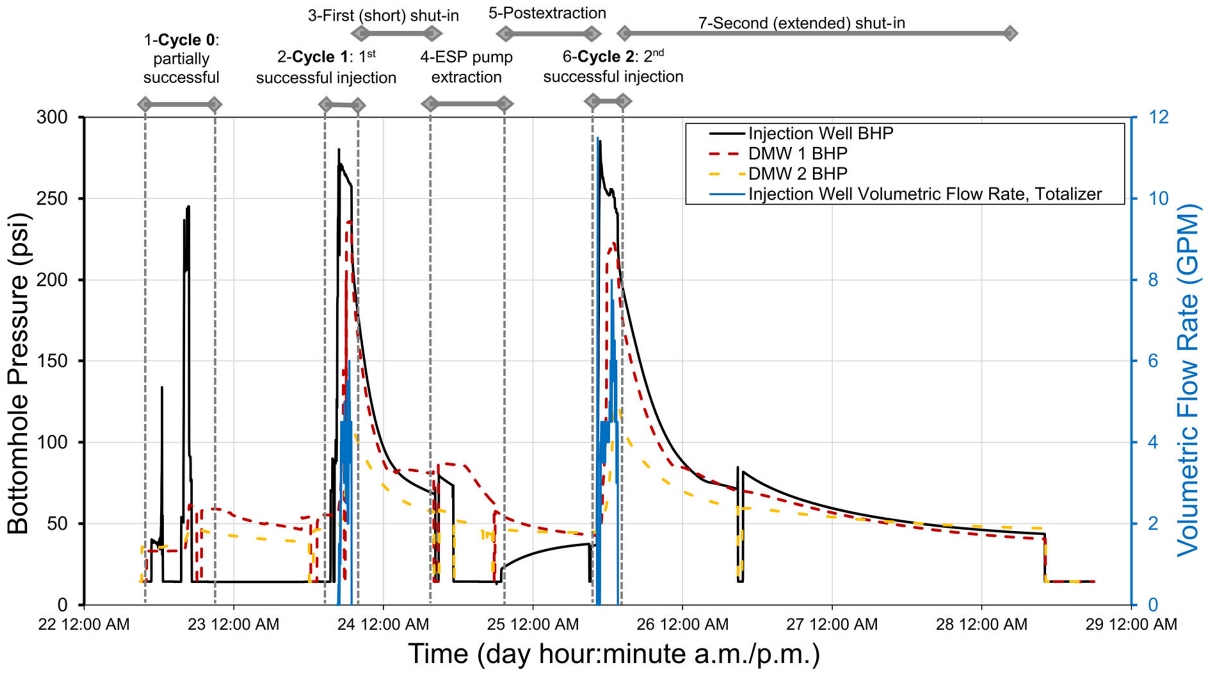

Fig. 3. (left axis) BHP recordings for injection well, DMW 1, and DMW 2. (right axis) Totalizer-based volumetric-flow rate at injection well, through 1 week of injection and shut-in. BHP = bottomhole pressure at fracture mouth in injection well or expected fracture opening in monitoring wells, at a depth of 53.34 m (175 ft). During two time periods in which recorded pressure remained level at 97.95 kPa (14.2 psi), injection-well pressure transducer was removed from well and kept at ground surface. Prior to 16.47 on September 23, the volumetric injection rate was below 1 GPM and not recordable by the totalizer.

Nonzero flow rates were recorded only after the wellhead pressure exceeded 1.172 MPa (170 psi). We think that the fluid flow was received mainly by the horizontal fracture because (1) wellhead-pressure gauges in DMW 3 and 4 which are open to the formation only at a 39.62- to 42.67-m (130- to 140-ft) depth interval did not register any pressure spikes and (2) the high-pressure front was detected at the DMW 1 and DMW 2 wellheads in less than 1 hour. The delay in peak of pressure for DMW 1 and 2 as compared with that of the injection well is attributable to a lag in pore-pressure diffusion from the injection well toward the monitoring wells through fluid flow in the packed and reopened horizontal fracture.

Cycles 1 and 2 provided cross-validation data for hydrogeological-model history matching. Because of the quality of data on September 25 which was higher than that on September 23, the poroelastic model was constructed based on data on September 25 only. This difference in data quality was mainly because of no water leakage on September 25 and observed water leakage from DMW 1 on September 23.

3. METHOD

3.1. *Numerical Approach*

Our hydrogeological model in the CMG (Computer Modelling Group, 2020) GEM™ package uses a finite-difference scheme to solve the conservation of mass and Darcy-based, single-phase fluid flow in a single-continuum (i.e., single-porosity, single-permeability) domain. The outcomes of simulating a water-injection scenario using this model are a change of pore pressure and salinity. To improve numerical convergence at high injection rates, this model can benefit from a fully implicit scheme in solving governing equations.

Our fully-coupled poroelastic model in the Abaqus software program (Dassault Systèmes, 2017) solves for change in poroelastic stresses and strains, pore pressure, and fracture reopening through quasistatic analyses. A Lagrangian, finite-element mesh is connected to the porous media, and effective stress in this domain is governed not only by stress and pore-pressure and flow-boundary conditions, but also by gravitational-body forces and a Darcy-based, single-phase fluid flow through this Lagrangian mesh. To simulate fracture reopening and growth, we used a cohesive-zone model, which simplifies the complex and microscopic process of fracture nucleation, coalescence, and propagation. This simplification has become possible by incorporation of a macroscale cohesive law consisting of an elastic linear response prior to fracture initiation, followed by assessment of a progressive-damage response after satisfaction of a fracture-initiation criterion (Haddad et al., 2017). The fracture-initiation criterion in this model is maximum principal stress, and fracture propagation is governed by a Benzeggagh-Kenane energy model, as practiced by Haddad and Sepehrnoori (2015) and Haddad et al. (2017).

3.2. *Hydrogeological Model Construction*

The hydrogeological model was built under the following assumptions: (1) it would be a layer-cake model with a simplified flat shape and geometry of the modeled area of interest, (2) reservoir conditions and properties would be considered uniform within each layer at the same depth, (3) an open reservoir boundary would account for an infinite reservoir relative to the small modeled area, and (4) a fully saturated formation would lie below the water level at a 39.62-m (130-ft) depth. We used DFPS core and fracturing data to tune model parameters.

This layer-cake model and gridding system, along with relative locations of wells, and the hydraulic fracture geometry at 53.34-m (175-ft) depth are shown in **Fig. 2**. A tartan gridding system was used to capture fluid-flow details near the wells without adding too much computational burden to the whole system.

We used the DFPS core and fracturing data to tune the model parameters initially. These reservoir properties are listed in **Table 1**.

Table 1. Common parameters used in both hydrogeological and poroelastic models. Values in brackets = oilfield units. Cases 1 through 6 refer to poroelastic simulation cases with different values of the input parameters.

Property	Value	
	Hydrogeological model	Poroelastic model
Formation permeability^{*+}, k_f (m^2) [mD]	9.87×10^{-15} [10]	1.48×10^{-16} [0.15] (Cases 1–3, 5, 6); 9.87×10^{-15} [10] (Case 4)
Open-fracture permeability*, k_{frac} (m^2) [D]	1.78×10^{-11} [18] in area in Fig. 2b	Solution-dependent
Propped-fracture permeability*, k_{prop} (m^2) [D]	7.90×10^{-12} [8] in area in Fig. 2b	Solution-dependent
Porosity^{+}, ϕ (dimensionless)	0.19	0.23
Pore-pressure gradient$^{\&}$, $\partial P_p / \partial z$ (kPa/m) [psi/ft]	9.80 [0.433]	4.53 [0.2]
Water-table depth, d_{wt} (m) [ft]	38.7 [127]	0 [0]
Water saturation, S_w (dimensionless)	0.99$^{\#}$	1
Water viscosity, μ_f (Pa.s) [cp]	10^{-3} [1]	10^{-3} [1]

*, $^{+}$ = history-matching parameters in hydrogeological and geomechanical models, respectively.

$^{\#}$ = For numerical stability of hydrogeological model, water saturation was set up slightly less than 1.

$^{\&}$ = The difference in pore-pressure gradient in hydrogeological and poroelastic models is explained in section 3.3.

During fracture reopening, hydraulic-fracture permeability changes substantially. We assumed three steps for this fracture reopening: steps 1 and 3 which resemble a closed fracture filled with proppants; and step 2 which represents fracture reopening with a substantial change in fracture permeability through time (**Fig. 4**). During the history matching process, these steps were simulated in the hydrogeological model through a change in fracture permeability (see section 3.4).

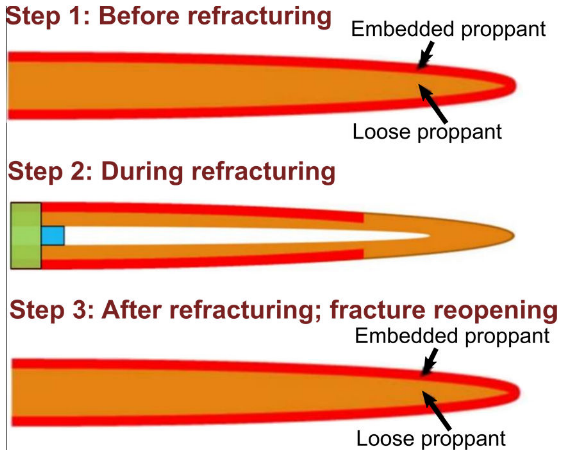

Fig. 4. Three steps occurring in one refracturing cycle (modified after Yi et al., 2019). Due to low flow rates employed in the study, we assume that the hydraulic fracture is not extended beyond the current fracture area and is rather dilated only within a smaller area than the total propped area.

3.3. *Poroelastic Model Construction*

To model reopening of a horizontal hydraulic fracture at this site, we assumed a horizontal cohesive layer with zero thickness, between 53.34-m (175-ft) thick upper and lower rock layers (**Fig. 5**). We modeled a triaxial stress state by directly loading three lateral boundaries according to minimum and maximum horizontal stresses. Because the model extended to the ground surface, the boundary overburden stress on top of the model at the ground surface is zero. This model consists of (1) 101,292 linear, hexahedral C3D8P elements with pore-pressure degrees of freedom representing porous rock and (2) 2,202 COH3D8P pore-pressure cohesive elements, representing the fracture domain. The total number of nodes and degrees of freedom are 109,907 and 439,628, respectively.

This model assumes fully saturated media, leading to the water table at the ground surface. To correct the pore-pressure value at fracture depth following this assumption, we reduced the pore-pressure gradient to 4.53 kPa/m (0.2 psi/ft), resulting in an initial BHP of 241.469 kPa (35 psi) at fracture depth, as measured before the injection experiments. This pore pressure is consistent with that in the hydrogeological model because the hydrogeological model assumes the actual water-table depth of 38.7 m (127 ft). The parameters specific to the geomechanical model are listed in **Table 2**.

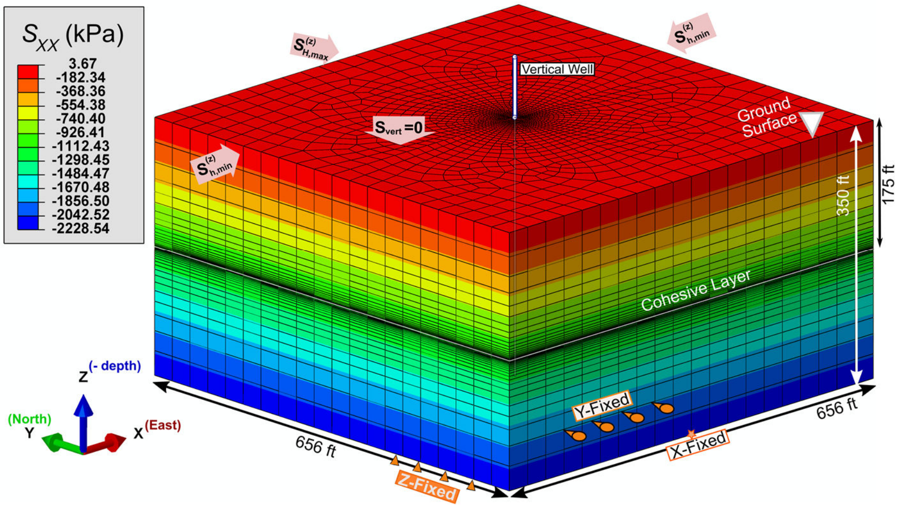

Fig. 5. Poroelastic model geometry with details of boundary conditions and vertical injection well. Contours show normal effective stress component in x-direction (east-west), aligned with $S_{h,\min}$ azimuth. Horizontal hydraulic fracture reopens over horizontal cohesive layer initiating from intersection of vertical well and cohesive layer.

Table 2. Parameters specific to the poroelastic model. Values in brackets = oilfield units. Large leakoff coefficient adopted because injected water did not contain any common hydraulic-fracturing fluid additives, such as viscosifying or cross-linking agents.

Parameter	Value
Young's modulus⁺, E (MPa) [psi]	689.75 [10^5]
Poisson's ratio, ν (dimensionless)	0.1
Water-bulk modulus, K_w (MPa) [psi]	2,150 [311,705]
Biot-Willis coefficient, α_{B-W} (dimensionless)	0.9
Dry-rock-bulk modulus, K_d (MPa) [psi]	287 [41,667]
Grain-bulk modulus, K_g (MPa) [psi]	2,874 [416,667]
Fracture toughness, K_I (MPa.$\sqrt{m}$) [psi.$\sqrt{in}$]	1.02 [929.4]
Fracture-initiation stress⁺, σ_{init} (kPa) [psi]	413.85 [60] (Cases 1–4); 137.95 [20] (Case 5); 689.75 [100] (Case 6)
Energy-release rate, G_I (kN/m) [lbf/in]	1.498 [8.552]
Initially open fracture area⁺, A_{init} (m^2) [ft^2]	100 [1076.4] (Case 1, 4-6); 28 [301.4] (Case 2); 400 [4305.6] (Case 3);
Leakoff coefficient, α_l (m^3/kPa.s) [Gal/psi.s]	0.2 [364.4]
Friction coefficient, μ_s (dimensionless)	0.3
Generalized Angelier's shape parameter, A_φ (dimensionless)	2.5
S_{vert} gradient⁺, $\partial S_{\text{vert,tot}}/\partial z$ (kPa/m) [psi/ft]	24.52 [1.08] (Cases 1–5); 20.37 [0.9] (Case 6)
$S_{h,\min}$ gradient⁺, $\partial S_{h,\text{min,tot}}/\partial z$ (kPa/m) [psi/ft]	32.20 [1.42] (Cases 1–5); 26.37 [1.16] (Case 6)
$S_{H,\max}$ gradient⁺, $\partial S_{H,\text{max,tot}}/\partial z$ (kPa/m) [psi/ft]	39.88 [1.76] (Cases 1–5); 32.37 [1.43] (Case 6)
Gravitational acceleration, g (m/s^2) [ft/s^2]	9.81 [32.18]

⁺ = additional history-matching parameters used in tuning the geomechanical model.

3.4. Estimation of Hydromechanical Properties

Our model construction required an estimate of the following parameters: petrophysical properties (e.g., porosity, permeability, and density), rock-mechanical properties (e.g., Young's modulus, Poisson's ratio, water-bulk modulus, dry-rock-bulk modulus, grain-bulk modulus, fracture-initiation stress, fracture toughness, and energy-release rate), leakoff coefficient, and in-situ stresses (Tables 1, 2). We obtained primary estimates of porosity, permeability, density, Young's modulus, and Poisson's ratio from an unpublished, internal report (Gonzalez et al., 2016) from core plug samples from DFPS, and estimated the fracture-energy release rate from the Irwin (1957) plane-strain theory:

$$G_I = K_I^2(1-\nu^2)/E, \tag{1}$$

where K_I, ν, and E denote fracture toughness, hosting rock Poisson's ratio, and Young's modulus, respectively. Through history matching of the BHP, we obtained the fracture toughness of 1.02 MPa.$\sqrt{m}$ (929.4 psi.$\sqrt{in}$) and fracture-initiation stress of 413.85 kPa (60 psi) (Table 2).

The dry-rock bulk modulus was estimated as

$$K_d = E/3(1-2\nu). \tag{2}$$

The grain-bulk modulus was obtained as

$$K_g = K_d/(1-\alpha_{B-W}), \tag{3}$$

where α_{B-W} denotes the Biot-Willis coefficient (Table 2). The dry-rock density was estimated as

$$\rho_d = \partial S_{\text{vert,tot}}/\partial z - \phi\rho_w, \tag{4}$$

where $\partial S_{\text{vert}}/\partial z$ denotes total-vertical-stress gradient (i.e., overburden or lithostatic-stress gradient), ϕ is porosity, and ρ_w represents water density (Table 2). To reduce the computational expenses of poroelastic simulations, we did not model the pressure drop within perforations; however, we calculated the pressure drop in psi on the basis of an equation proposed by McClain (1963):

$$\Delta P_{perf} = 0.2369 Q^2 \rho / C_d^2 N^2 D^4, \tag{5}$$

where Q denotes flow rate in bbl/min, ρ is density in lb/gal, C_d represents discharge coefficient, N is number of perforations, and D is perforation hole diameter in inches. C_d is assumed to be 0.63, according to the perforation geometry in this project (Grose, 1985); one perforation hole is assumed, and perforation diameter is 0.01 m (0.4 inch). Although we assumed only one perforation hole with a relatively small diameter, the maximum pressure drop through the perforation in none of the simulation cases exceeded 6 psi, which is almost 4% of the minimum principal stress at 53.34-m (175-ft) depth. We therefore neglected the perforation pressure drop in this modeling study.

As noted in the introduction, the hydrogeological model does not solve for stress-dependent, dynamic-fracture reopening. To include the effect of fracture reopening on the hydrogeological-model results, we needed to set up a time-dependent fracture permeability that increases substantially only during fracture dilation. The permeability of a propped hydraulic fracture is markedly higher than the permeability of the host rock, although still much lower than an open, proppant-free fracture conduit (e.g., 8.3×10^{-10} m^2 or 844 Darcy for a 0.1-mm wide fracture opening, according to $d^2/12$ with d denoting the proppant-free fracture aperture). We estimated propped-fracture permeability in m^2 units after Barree et al. (2019):

$$k_{prop} = \frac{d_p^2}{180} \frac{\phi^3}{(1-\phi)^2}, \tag{6}$$

where d_p is proppant diameter in meters and ϕ denotes proppant pack porosity. For U.S. mesh 140, d_p is about 105 microns (0.105×10^{-3} m), and ϕ is in the range of 0.26 to 0.44 corresponding to a proppant pack of closely packed hexagonal morphology to loosest possible random packing of mechanically connected particles (Jaeger and Nagel, 1992). The ϕ can increase to 0.47 for a structured cubic-lattice structure (Barree et al., 2019). The expected value of ϕ for a proppant pack of a random, close-packed, hard, spherical grains is 0.36 (Jaeger and Nagel, 1992). These parameters led to proppant-pack permeability values of 1.97×10^{-12} to 2.27×10^{-11} m^2 (2 to 23 Darcy). Knowing only a plausible range for these permeabilities, we tuned propped fracture permeability, as well as matrix permeability and open-fracture permeability, through history matching. The propped-fracture boundary in plan view is fixed in this model (**Fig. 2b**).

3.5. In-Situ Pore Pressure and Stresses

The original BHP at a fracture depth of 53.34 m (175 ft) was estimated from the water-table level at 38.71 m (127 ft) below ground surface in the injection well measured on September 16, 2020, assuming hydrostatic conditions. This measurement led to 241.469 kPa (35 psi) original BHP, which assumed a water density of 1,000 kg/m^3, a gravitational acceleration of 9.81 m/s^2, and atmospheric pressure of 97.945 kPa (14.2 psi).

The hydraulic fracture at the DFPS is horizontal, and the minimum principal stress is the stress component normal to the fracture plane; in this case, the stress is overburden (lithostatic) stress, S_{vert}, at a 53.34-m (175-ft) depth. This principal stress is of utmost importance for fracture growth, reopening, and closure, and integration of a density log through depth could lead to a direct measurement of this principal stress. Unfortunately, no density log was available for this site. To estimate this principal stress indirectly, we used two methods to analyze the collected bottomhole-injection-pressure data during shut-in periods. Both methods assume that water pressure within the fracture is at equilibrium, with the principal stress normal to the fracture plane. These methods are the (1) tangent method and (2) *G*-function method, which are based on concepts developed for a diagnostic fracture-injection test. For hydraulic-fracture reopening, BHP should exceed S_{vert}. During the shut-in period and at the moment of fracture closure, BHP converges to S_{vert} again, which is known as *fracture closure pressure* (FCP).

A first analysis consists of drawing two lines tangential to post-shut-in BHP data, one tangent to the pressure profile immediately after shut-in and the second tangent to the pressure profile once the pressure profile deviates from this sharp decline (**Fig. 6**). Fluid pressure associated with the intersection of these two lines represents instantaneous shut-in pressure (ISIP) corresponding to the point at which the friction drag is eliminated following closure of the wellhead shutoff valve. This analysis resulted in ISIP equal to 1.448 MPa (210 psi) and may denote an upper bound for FCP. The identical pressure values obtained by this tangent method during the first and second shut-in periods show the independence of ISIP from operational conditions. Provided that we assume a negligible difference between ISIP and FCP, the overburden-stress gradient can be estimated at 27.156 kPa/m (1.2 psi/ft), obtained by dividing 1.448 MPa (210 psi) by the fracture depth of 53.34 m (175 ft).

The second method is *G*-function analysis, which helps in identifying fracture-closure time the moment when $G.\partial P/\partial G$ deviates from a linear trend. G is a dimensionless time (i.e., *G*-time) and is calculated by

$$G = (4/\pi)\big(g(\Delta t_D) - g(0)\big), \tag{6}$$

$$g(\Delta t_D) = (4/3)\big((1+\Delta t_D)^{1.5} - \Delta t_D{}^{1.5}\big), \tag{7}$$

$$\Delta t_D = \big(t - t_p\big)/t_p, \tag{8}$$

where t denotes current time, t_p is total pumping time, P represents BHP, and $\partial P/\partial G$ is *G*-time derivative of BHP (Fekete Inc., 2014). We calculated $G.\partial P/\partial G$ at point i numerically using a central discretization scheme as

$$G_i\,(P_{i+1} - P_{i-1})/(G_{i+1} - G_{i-1}), \tag{9}$$

where indices i+1 and i-1 correspond to a time step after or before the current time step i, respectively. In this analysis, $G.\partial P/\partial G$ is plotted versus G-time, and a line passing through the origin is drawn tangential to the $G.\partial P/\partial G$ plot to obtain the deviation of $G.\partial P/\partial G$ from a linear trend (**Fig. 7**). Accordingly, FCP occurred at 4:50 p.m. on September 25 and is equal to 1.066 MPa (154.536 psi). This time is almost 3 hours after the recording of ISIP during this shut-in period. This analysis shows that (1) compared with ISIP, BHP needed to drop for an extra 344.877 kPa (50 psi) to lead to fracture closure and (2) fracture closure does not occur instantaneously after shut-in and is a relatively slow process. This slow fracture-closure process can be caused either by the small fluid-leakoff rate or small-rock permeability. The G-function analysis resulted in an overburden-stress gradient of 20.367 kPa/m (0.9 psi/ft).

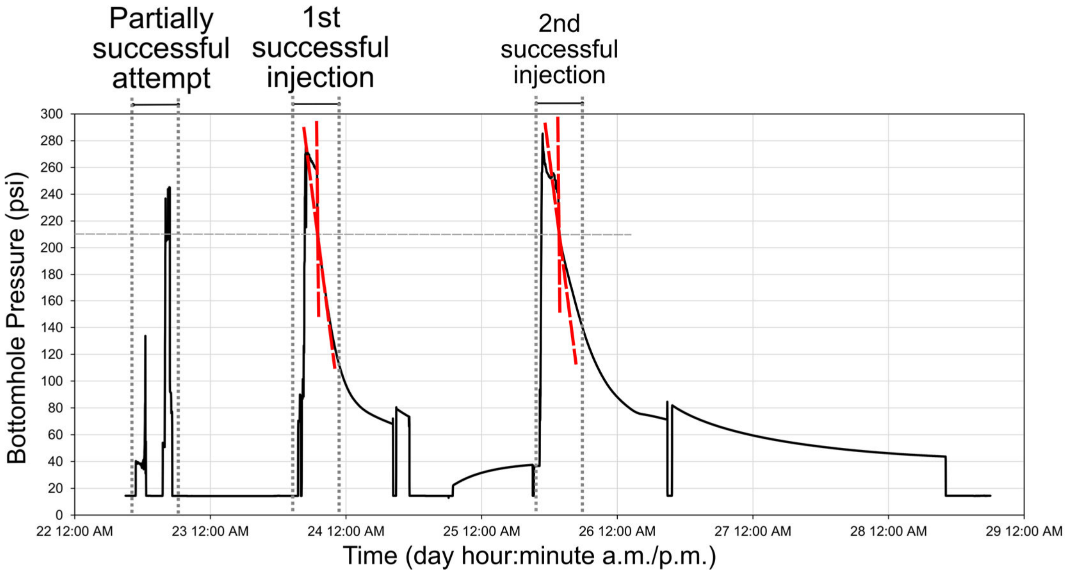

Fig. 6. Injection-well BHP versus time. Time interval on abscissa is from September 22 to September 29, 2020, represented by numbers 22 through 29 for brevity, and time is recorded on the basis of U.S./Texas central daylight time. Intersection of lines tangential to post-shut-in BHP evolution shows ISIP, which can be interpreted as FCP or overburden stress over horizontal hydraulic fracture.

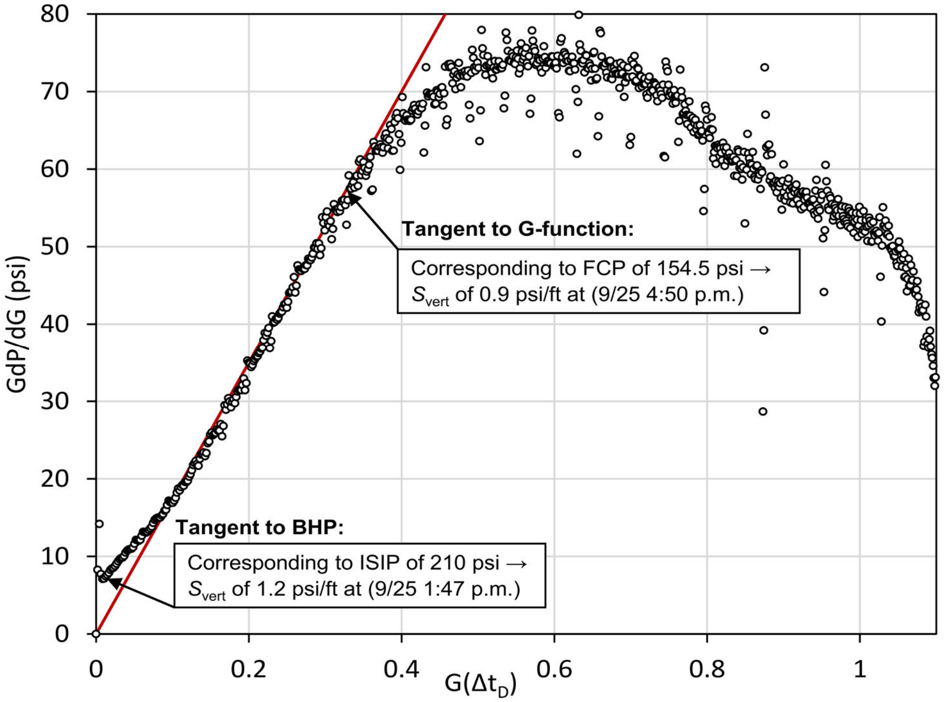

Fig. 7. G-function pressure analysis. Black circles = $G.\partial P/\partial G$, which are based on field data collected on September 25, 2020, and red line = a straight line drawn from origin and tangent to trend followed by black circles. FCP = point where black-circle trend deviates from linear red line. Instantaneous shut-in pressure (ISIP), obtained from Fig. 6, corresponds to data point much earlier than that for FCP.

Through a history-matching analysis to obtain BHPs close to recorded values, we reached an overburden-stress gradient of 24.525 kPa/m (1.08 psi/ft), which is an intermediate value between values suggested by tangent and *G*-function methods. Also, this value is consistent with an upper bound of clay-rich, sandstone-rock density reported by Gonzalez et al. (2016).

On the basis of the procedure described by Haddad and Eichhubl (2020), we obtained horizontal stresses following assumptions for the friction coefficient, μ_s, and a generalized Angelier's shape parameter, A_φ (Simpson, 1997). On the basis of the outcomes of triaxial tests by Gonzalez et al. (2016), we assumed a small μ_s of 0.3, which is also supported by an abundance of friction-reducing, clay-rich minerals in this field. Knowing that the hydraulic fracture in our site is horizontal and, hence, under a reverse-faulting stress regime, we assumed A_φ equal to 2.5, which is the average value of this parameter in this stress regime.

3.6. History-Matching Procedure and Parameters

The field data collected for our history-matching analyses included injection rate and BHP. During this analysis of the hydrogeological model, we varied formation and fracture permeability. We first matched injection-well BHP with field data for the injection well and DMW 1 and 2 during Cycle 2 (**Fig. 3**). Then, to validate the matched parameters, we used the updated model to solve for BHP data for the same wells during Cycle 1. We achieved the best history-matched solution through adjustment of one parameter (e.g., fracture permeability) at one time to match the BHP in one of the wells. This adjustment was then applied to other wells, and further adjustment was made for the second parameter (e.g., matrix permeability) to match BHP in those wells. Hundreds of simulations were performed to match all field data. On the basis of core-permeability measurements from prior lab studies, we began by using a matrix-permeability value of 9.87 × 10^{-15} m^2 (10 mD; Gonzalez et al., 2016) and proceeded to change it slightly to match the new field results in Cycle 2. To better match the field data, the closed-propped-fracture permeability was varied between 6.91×10^{-12} and 8.88×10^{-12} m^2 (7 and 9 Darcy), and opened-fracture permeability was varied between 1.97×10^{-11} and 7.90×10^{-11} m^2 (20 and 80 Darcy) spatiotemporally during fracture reopening.

The history-matching parameters of the poroelastic model were formation permeability, fracture-initiation stress, and overburden-stress gradient. Considering that fracture area and aperture are solution variables in the poroelastic model, we did not need to assume fracture permeability as an input parameter in the poroelastic model. Also, on the basis of the method for estimation of in-situ stresses (section 3.5), we adjusted horizontal stresses by changing the overburden-stress gradient.

4. HISTORY MATCHING RESULTS

Hydrogeological simulations resulted in the best set of input parameters for minimizing the discrepancy between BHP in the injection well and DMW 1 in Cycle 2 injection (**Figs. 8** and **9,** respectively). This fitted parameter set is shown in Table 1. Subsequently, robustness of parameter adjustments in the history-matched model was evaluated through change of injection flow rate to Cycle 1 data. This evaluation revealed that the history-matched model is suitable for prediction of BHP during both Cycles.

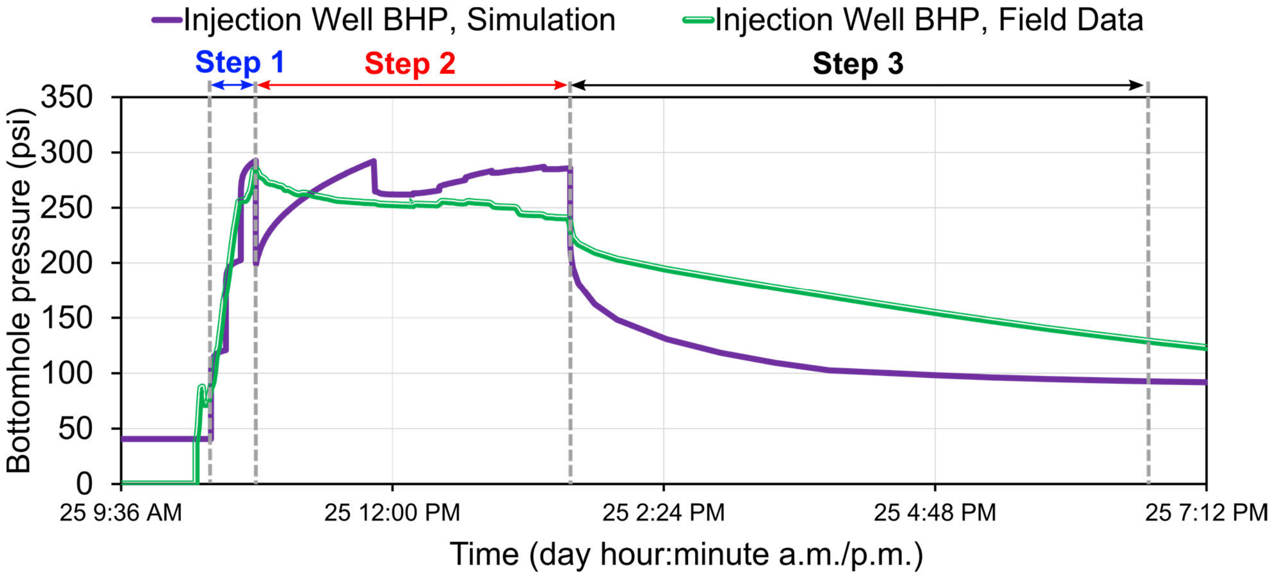

Fig. 8. History matching of BHP in injection well during Cycle 2. Main parameter to adjust for history matching is fracture permeability. Propped-fracture permeability of 6.91×10^{-12} to 8.88×10^{-12} m^2 (7 to 9 Darcy) used for Steps 1 and 3, and opened-fracture permeability used for Step 2 when area of opening fracture changes linearly. Fracture permeability variation between steps validated by comparison of BHP from field data and simulation in DMW 1 during Cycle 2 (Fig. 9).

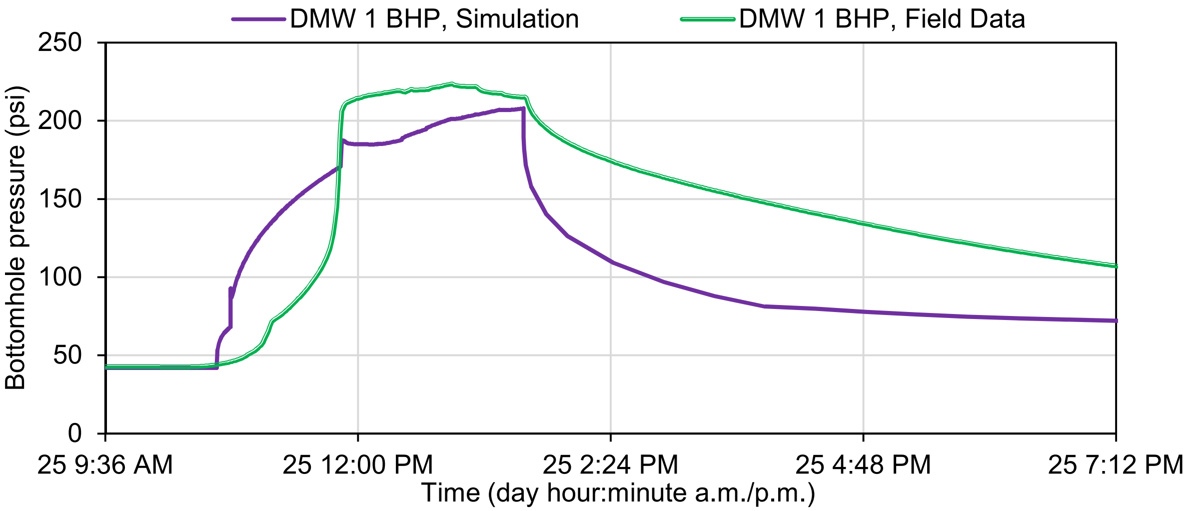

Fig. 9. History matching of BHP in DMW 1 during Cycle 2, September 25, 2020.

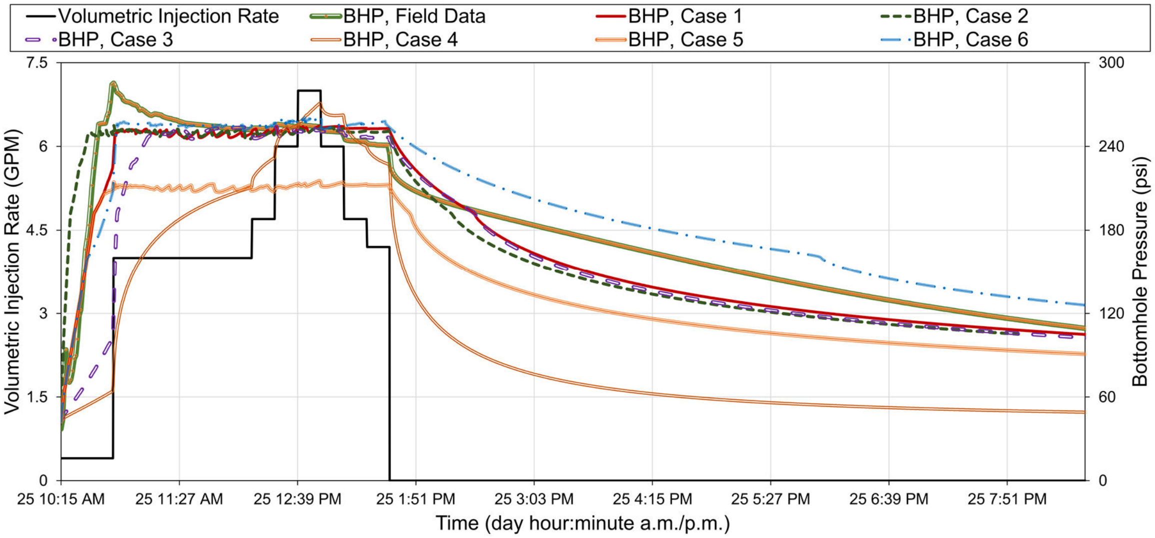

Fig. 10. (left axis) Volumetric flow rate; (right axis) BHP from field data versus six poroelastic simulation cases. These cases differ in (1) size of initially open area of the hydraulic fracture: 100 m^2 (Case 1, 4–6), 28 m^2 (Case 2), 400 m^2 (Case 3); (2) fracture-initiation stress: 413.85 kPa (Cases 1–4), 137.95 kPa (Case 5), 689.75 kPa (Case 6); and (3) overburden-stress gradient: 24.52 kPa/m (Cases 1–5); 20.37 kPa/m (Case 6). BHP recorded by transducer compared with BHP within the well bore, calculated by adding perforation pressure drop to simulated fracture-mouth pressure.

A sample set of poroelastic-model results out of 51 simulations is illustrated in **Fig. 10.** This figure compares BHP from field data and six simulation cases, differing in initially open area of hydraulic fracture, A_{init}; formation permeability, k_f; fracture initiation stress, σ_{init} ; and overburden-stress gradient, $\partial S_{\text{vert,tot}}/\partial z$. BHP is only slightly sensitive to A_{init}. Comparing Cases 1, 2, and 3 shows that Case 1 with A_{init} of 100 m^2 leads in more closely matching field data for BHP at early times. Comparing Case 1, with a k_f of 1.48×10^{-16} m^2 (0.15 mD), and Case 4, with a k_f of 9.87×10^{-15} m^2 (10 mD), shows that matching of post-shut-in BHP requires using sub-mD-formation permeability values. Comparing Cases 1 and 5 shows that reducing fracture-initiation stress, σ_{init}, by one-third substantially reduces BHP, although the initially open-fracture area is the same in these two cases. Comparing Cases 1 and 6 at different $\partial S_{\text{vert,tot}}/\partial z$ shows that increasing σ_{init} from 413.85 kPa (60 psi) to 689.75 kPa (100 psi) leads to larger BHPs, especially during post-shut-in, despite the fact that the overburden-stress gradient has dropped from 24.52 kPa/m (1.08 psi/ft) to 20.37 kPa/m (0.9 psi/ft). These data illustrate the dominant effect of σ_{init} as compared with $\partial S_{\text{vert,tot}}/\partial z$ on BHP. Given other simulation results, which are not shown here, injection pressure is also sensitive to Young's modulus, and a more compliant formation leads to a better simulation match with BHP from the field data. Using a low value for Young's modulus, 689.75 MPa (10^5 psi), is also justified because rocks at fracture depth are friable.

Overall, the simulation result closest to BHP data belongs to Case 1, with an A_{init} of 100 m^2 (1,076.4 ft^2), a k_f of

1.48×10^{-16} m^2 (0.15 mD), a σ_{init} of 413.85 kPa (60 psi), and a $\partial S_{\mathrm{vert,tot}}/\partial z$ of 24.52 kPa/m (1.08 psi/ft). The early-time pressure response, however, needs further numerical study with improved volumetric-rate measurements because the totalizer measurements below 6.309×10^{-5} m^3/s (1 GPM) were unreliable.

The formation-permeability value of 1.48×10^{-16} m^2 (0.15 mD) offered by these models is substantially lower than that by the hydrogeological models, but it is consistent with the sub-mD-permeability measurements of the regional cores by Gonzalez et al. (2016). To obtain a history match during the extended shut-in period, we had to lower formation permeability substantially. The slight difference in inclusion of dynamic fracture-permeability changes in our hydrogeological and poroelastic models suggests fracture permeability as the most critical parameter that influences the BHP history matching.

The second most critical parameter in estimation of the BHP is the overburden stress gradient. In this work, we estimated this parameter on the basis of temporal BHP changes. However, our current field studies include density logging from the surface to the fracture depth to directly calculate the overburden stress gradient.

Fracture and rock characterization in this work is founded on bottomhole-pressure and flow-rate measurements and calibration of the input parameters in the hydrogeological and poroelastic models. The uncertainties in numerous input parameters would likely reduce in case additional downhole measurements such as borehole deformation are adopted, for instance using three-dimensional deformation units (Guglielmi et al., 2014). However, considering that the targeted injection zone is a preexisting horizontal fracture and with access to the lab-measured rock mechanical properties, the integration of the presented modeling efforts seems adequate to fulfill our current goals in understanding injection-induced changes of an existing hydraulic fracture.

5. CONCLUSIONS

The quality of the data collected during field deployment in September 2020 allowed us to define benchmark cases for performing history matching of our hydrogeological and geomechanical models. Repeatability of injection experiments and fracture dilation were demonstrated through matching of ISIP during the first and second successful injection cycles. This reproducibility was also shown by the small observed difference between maximum injection pressures as a fracture characteristic during these cycles. With access to field and petrophysical and geomechanical lab data, we were able to tune hydromechanical reservoir parameters of the models to result in a history-matched BHP. Discrepancy between estimated permeability by hydrogeological and geomechanical models originated from (1) their different methods of modeling fracture reopening; (2) possible poroelastic rock behavior, which was neglected in the hydrogeological model; and (3) difference in the time intervals in which history-matching analyses of these models were conducted.

The computational models that were developed are essential for designing future injections at the DFPS and for the interpretation of various electromagnetic surveys we have already collected. In our subsequent papers, we will demonstrate the utility of EM contrast agents for the measurement of flow, salinity, and pore pressure inside a contrast-agent-filled fracture under various hydromechanical and geochemical conditions.

6. ACKNOWLEDGMENTS

This work was supported by the U.S. Department of Energy, Office of Fossil Energy, National Energy Technology Laboratory under Award Number DE-FE0031785, and the State of Texas Advanced Oil and Gas Resource Recovery program at the Bureau of Economic Geology. We would like to thank the Advanced Energy Consortium's member companies, including ExxonMobil, Repsol, Shell, and Total. We also thank Héctor González, Jacobo Canal, and Ricardo Melo of Repsol for providing the geomechanical measurements of core plugs from the DFPS and Geoprojects International, Inc. for performing the hydrological operations at the DFPS. We acknowledge Dassault Systèmes Simulia Corp. and Computer Modelling Group Ltd. for providing the academic Abaqus and CMG licenses and Texas Advanced Computing Center for supporting high-performance computing. Publication authorized by the Director, Bureau of Economic Geology, The University of Texas at Austin.

REFERENCES

1. Ahmadian, M., D. LaBrecque, Q.H. Liu, A. Kleinhammes, P. Doyle, Y. Fang, G. Jeffrey, and C. Lucie. 2019. Validation of the utility of the contrast-agent-assisted electromagnetic tomography method for precise imaging of a hydraulically induced fracture network. In *Proceedings of the SPE Annual Technical Conference and Exhibition, Calgary, Alberta, Canada, 30 September–2 October 2019.* SPE-196140-MS. DOI: 10.2118/196140-MS.
2. Ahmadian, M., D. LaBrecque, Q.H. Liu, W. Slack, R. Brigham, Y. Fang, K. Banks, Y. Hu, D. Wang, and R. Zhang. 2018. Demonstration of proof of concept of electromagnetic geophysical methods for high resolution illumination of induced fracture networks. In *Proceedings of the SPE Hydraulic Fracturing Technology Conference and Exhibition, The Woodlands, Texas, USA, 23–25 January 2018.* SPE-189858-MS. DOI: 10.2118/189858-MS.

3. Barree, R., R. Duenckel, and B.T. Hlidek. 2019. Proppant sieve distribution-what really matters? In *Proceedings of the SPE Hydraulic Fracturing Technology Conference and Exhibition, The Woodlands, Texas, USA, 5–7 February 2019*. SPE-194382-MS. DOI: 10.2118/194382-MS.

4. Cipolla, C.L. and C.A. Wright. 2000. State-of-the-art in hydraulic fracture diagnostics. In *Proceedings of the SPE Asia Pacific Oil and Gas Conference and Exhibition, Brisbane, Australia, 16–18 October 2000.* SPE-64434. DOI: 10.2118/64434-MS.

5. Computer Modelling Group Ltd. 2020. GEM compositional & unconventional simulator user guide, volume 2020.10. Calgary, Canada.

6. Dassault Systèmes. 2017. Abaqus analysis user's guide, volume 2017. Waltham, Massachusetts.

7. Denison, J., L. Murdoch, D. LaBrecque, and W. Slack. 2015. Electrical and magnetic imaging of proppants in shallow hydraulic fractures. In *Proceedings of AGU Fall Meeting, San Francisco, California, USA, 14–18 December 2015*. NG-13A-1872.

8. Fang, Y., J. Dai, Q. Zhan, Y. Hu, M. Zhuang, and Q.H. Liu. 2019. A hybrid 3D electromagnetic method for induction detection of hydraulic fractures through a tilted cased borehole in planar stratified media. *IEEE Geoscience and Remote Sensing Letters* 15(7): 996–1000. DOI: 10.1109/TGRS.2019.2891674.

9. Fekete Inc. 2014. Minifrac pre-closure analysis. Available at: http://www.fekete.com/san/webhelp/welltest/webhelp/Content/HTML_Files/Analysis_Types/Minifrac_Test_Analyses/Minifrac-Pre-Closure_Analysis.htm (accessed December 22, 2020).

10. Gonzalez, H., J. Canal, P. Fernandez, M.A. Ruano, and T. Workut. 2016. Geomechanical and petrophysical characterization for Wilson-9 plugs. *Internal Report,* Repsol Technology Centre, G.D. Strategy and Control.

11. Grose, R.D. 1985. Orifice contraction coefficient for inviscid incompressible flow. *Journal of Fluids Engineering* 107(1): 36–43. DOI: 10.1115/1.3242437.

12. Haddad, M. and P. Eichhubl. 2020. Poroelastic modeling of basement fault reactivation caused by saltwater disposal near Venus, Johnson County, Texas. In *Proceedings of the 54th U.S. Rock Mechanics / Geomechanics Symposium, Golden, Colorado, USA, 28 June–1 July 2020. ARMA-20-2006.*

13. Haddad, M., J. Du, and S. Vidal-Gilbert. 2017. Integration of dynamic microseismic data with a true 3D modeling of hydraulic-fracture propagation in the Vaca Muerta Shale. *SPE J.* 22(6): 1714–1738. SPE-179164-PA. DOI: 10.2118/179164-PA.

14. Haddad, M. and K. Sepehrnoori. 2015. Simulation of hydraulic fracturing in quasi-brittle shale formations using characterized cohesive layer: Stimulation controlling factors. *J. Unconventional Oil Gas Resources* 9: 65–83. DOI: 10.1016/j.juogr.2014.10.001.

15. Hu, Y., Y. Fang, D. LaBrecque, M. Ahmadian, and Q.H. Liu. 2018. Reconstruction of high-contrast proppant in hydraulic fractures with galvanic measurements. *IEEE Transactions on Geoscience and Remote Sensing* 56(4): 2066–2073. DOI: 10.1109/TGRS.2017.2773080.

16. Hu, Y., Z. Yu, W. Zhang, Q. Sun, and Q.H. Liu. 2016. Multiphysics coupling of dynamic fluid flow and electromagnetic fields for subsurface sensing. *IEEE Journal on Multiscale and Multiphysics Computational Techniques* 1: 14–25. DOI: 10.1109/JMMCT.2016.2559509.

17. Guglielmi, Y., F. Cappa, H. Lancon, J.B. Janowczyk, J. Rutqvist, C.F. Tsang, J.S.Y. Wang. 2014. ISRM suggested method for step-rate injection method for fracture in-situ properties (SIMFIP): Using a 3-component borehole deformation sensor. *Rock Mech Rock Eng* 47: 303-311. DOI: 10.1007/s00603-013-0517-1.

18. Irwin, G.R. 1957. Analysis of stresses and strains near the end of a crack traversing a plate. *Journal of Applied Mechanics–Transactions of ASME* 24: 351–369.

19. Jaeger, H.M. and S.R. Nagel. 1992. Physics of the granular state. *Science* 255(5051): 1523–1531. DOI: 10.1126/science.255.5051.1523.

20. LaBrecque, D., R. Brigham, J. Denison, L. Murdoch, W. Slack, Q.H. Liu, Y. Fang, J. Dai, Y. Hu, and Z. Yu. 2016. Remote imaging of proppants in hydraulic fracture networks using electromagnetic methods: Results of small-scale field experiments. In *Proceedings of the SPE Hydraulic Fracturing Technology Conference, The Woodlands, Texas, USA, 9–11 February 2016*. SPE-179170-MS. DOI: 10.2118/179170-MS.

21. McClain, C.H. 1963. Fluid flow in pipes: A clear-cut summary of modern theory in the flow of liquids and gases through piping and ducts, with practical applications and detailed worked-out examples. New York: The Industrial Press. https://hdl.handle.net/2027/mdp.39015000477268.

22. Simpson, R.W. 1997. Quantifying Anderson's fault types. *Journal of Geophysical Research* 102(B8): 17909–17919. DOI: 10.1029/97JB01274.

23. Stolyarov, S., E.Cazeneuve, K. Sabaa, D. Katz, and J. Yang. 2019. A novel technology for hydraulic fracture diagnostics in the vicinity and beyond the wellbore. In *Proceedings of the SPE Hydraulic Fracturing Technology Conference and Exhibition, The Woodlands, Texas, USA, 5–7 February 2019*. SPE-194373-MS. DOI: 10.2118/194373-MS.

24. Yi, S., R. Manchanda, M. Sharma, and N. Roussel. 2019. Preventing heel dominated fractures in horizontal well refracturing. In Proceedings of the SPE Hydraulic Fracturing Technology Conference and Exhibition, The Woodlands, Texas, USA, 5–7 February 2019. SPE-194341-MS. DOI: 10.2118/194341-MS.